Incoherent Cooper Pairing and Pseudogap Behavior in Single-Layer FeSe/SrTiO$_3$

B. D. Faeth,[1] S.-L. Yang,[1,2,3,*] J. K. Kawasaki,[1,2,†] J. N. Nelson,[1] P. Mishra,[1,‡]
C. T. Parzyck,[1] C. Li,[1] D. G. Schlom,[3] and K. M. Shen[1,2]

[1]*Department of Physics, Laboratory of Atomic and Solid State Physics, Cornell University, Ithaca, New York 14853, USA*
[2]*Kavli Institute at Cornell for Nanoscale Science, Ithaca, New York 14853, USA*
[3]*Department of Materials Science and Engineering, Cornell University, Ithaca, New York 14853, USA*

(Received 17 November 2020; revised 2 March 2021; accepted 13 April 2021; published 10 June 2021)

In many unconventional superconductors, the presence of a pseudogap—a suppression in the electronic density of states extending above the critical temperature—has been a long-standing mystery. Here, we employ combined *in situ* electrical transport and angle-resolved photoemission spectroscopy measurements to reveal an unprecedentedly large pseudogap regime in single-layer FeSe/SrTiO$_3$, an interfacial superconductor where incoherent Cooper pairs are initially formed above $T_\Delta \approx 60$ K but where a zero-resistance state is achieved only below $T_0 < 30$ K. We show that this behavior is accompanied by distinct transport signatures of two-dimensional phase fluctuating superconductivity, suggesting a mixed vortex state hosting incoherent Cooper pairs which persist well above the maximum clean limit T_c of approximately 40 K. Our work establishes the critical role of reduced dimensionality in driving the complex interplay between Cooper pairing and phase coherence in two-dimensional high-T_c superconductors, providing a paradigm for understanding and engineering higher-T_c interfacial superconductors.

DOI: 10.1103/PhysRevX.11.021054 Subject Areas: Condensed Matter Physics, Materials Science, Superconductivity

I. INTRODUCTION

Single-layer FeSe grown on SrTiO$_3$ (FeSe/SrTiO$_3$) has attracted interest due to its characteristics as an atomically thin, interfacially enhanced high-T_c superconductor. FeSe/SrTiO$_3$ exhibits a spectroscopic gap-opening temperature (T_Δ) between 60 and 70 K [1–4], nearly one order of magnitude higher than that of bulk FeSe (8 K) [5] and in excess of related electron-doped FeSe-based bulk compounds (approximately 40 K) [6,7]. The combination of its high T_c, relative simplicity, and inherently two-dimensional (2D) nature positions FeSe/SrTiO$_3$ as an ideal platform for exploring the importance of superconducting fluctuations and the possibility of interfacial enhancement in high-T_c materials.

Nevertheless, significant challenges impede the systematic study of FeSe/SrTiO$_3$, as its air sensitivity, variability in the postgrowth annealing process, and potential impact of capping layers make meaningful comparisons across different techniques and studies, both *in situ* and *ex situ*, difficult [8,9]. Consequently, there remains a widely observed but heretofore unexplained discrepancy between the gap-opening temperature T_Δ observed by angle-resolved photoemission spectroscopy (ARPES) ($T_\Delta \approx 60$ K) and the temperature at which a zero-resistance state has been measured by electrical transport, T_0 ($T_0 < 30$ K) [2,10–13]. A potential resolution to this puzzle is the existence of Cooper pair fluctuations above T_c, which are known to play an important role in two-dimensional superconductors as well as underdoped cuprates but have not been widely investigated for FeSe/SrTiO$_3$.

To reveal the intrinsic nature of superconductivity and the pseudogap in FeSe/SrTiO$_3$, we employ, for the first time, a combination of ARPES and *in situ* resistivity measurements to simultaneously probe both the spectroscopic and electrical transport properties of pristine single-layer FeSe/SrTiO$_3$ samples in ultrahigh vacuum. Through a systematic investigation of a large number of such samples, we reveal the presence of intrinsic superconducting

*Present address: Pritzker School of Molecular Engineering, University of Chicago, Chicago, Illinois 60637, USA.
†Present address: Department of Materials Science and Engineering, University of Wisconsin, Madison, Wisconsin 53706, USA.
‡Present address: Department of Physics, Indian Institute of Science, Bangalore 560012, India.

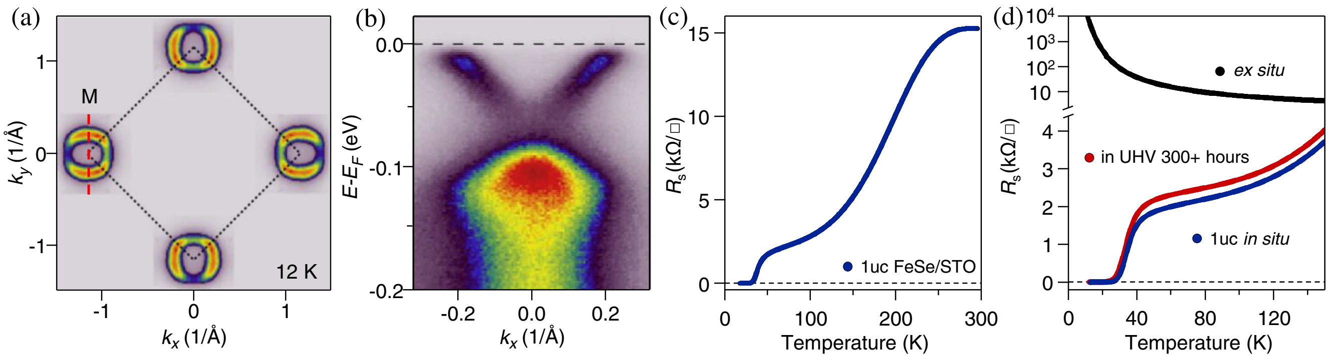

FIG. 1. Combined ARPES and *in situ* electrical resistivity measurement of single-layer $FeSe/SrTiO_3$. Measurements in (a)–(c) are conducted on the same sample. (a) Fermi surface intensity map for an as-grown 1 uc $FeSe/SrTiO_3$ sample held at 12 K, integrated over ±5 meV of E_F. The black dashed line indicates the boundary of the 2-Fe Brillouin zone. The electron pockets comprise 5.5% of the Brillouin zone area. (b) Photoemission intensity at M [dashed red line in (a)] taken at 12 K. (c) Temperature-dependent sheet resistance for 1 uc $FeSe/SrTiO_3$. (d) Stability of the superconducting state for a separate sample after growth (blue line), long-term UHV storage (red line), and after momentary exposure to an inert gas atmosphere (black line).

fluctuations over an unprecedentedly broad temperature range, as characterized by the window between the onset of spectroscopic gap T_Δ and the onset of zero resistance T_0. This result establishes the essential role that reduced dimensionality plays in the superconductivity of $FeSe/SrTiO_3$ and resolves the long-standing confusion surrounding the critical temperature of $FeSe/SrTiO_3$.

II. RESULTS

In Fig. 1, we show combined *in situ* resistivity and ARPES measurements conducted on the same sample of single-layer $FeSe/SrTiO_3$. The Fermi surface [Fig. 1(a)] is comprised of electron pockets centered at the M point consistent with an electron doping of $0.11e^-$ per unit cell, in good agreement with earlier reports [1,3,14], and exhibits the expected spectroscopic signatures of superconductivity (a well-defined gap and band backbending). Because of photoemission matrix elements in our measurement geometry, only one band is observed in the high-statistics cut shown in Fig. 1(b), despite the expectation of two nearly degenerate elliptical pockets at M [15]. In Fig. 1(c), we show the sheet resistance $R_s(T)$, which exhibits a humplike feature at 280 K, characteristic of heavily electron-doped bulk FeSe-derived compounds [16], and a broad superconducting transition which onsets at $T_{\mathrm{onset}} = 44 \pm 3$ K, eventually falling below 0.1% of $R_{70\,\mathrm{K}}$ at $T_0 = 29 \pm 0.2$ K. When measured *in situ*, $FeSe/SrTiO_3$ samples exhibit residual resistivity ratios (RRRs, defined as $R_{300\,\mathrm{K}}/R_{70\,\mathrm{K}}$) of approximately 10, in contrast to RRRs of approximately 1–2 for capped single-layer films reported in the literature [10]. While samples remain robust for hundreds of hours and over numerous cooling and warming cycles when maintained under ultrahigh vacuum [red curve, Fig. 1(d)], pristine films deteriorate instantaneously upon exposure to atmosphere [black curve, Fig. 1(d)].

To explore this behavior more systematically, we perform detailed temperature-dependent measurements of the energy gap $\Delta(T)$ using ARPES. In Fig. 2, we show a quantitative comparison between $\Delta(T)$ and $R_s(T)$ measurements on the same sample shown in Fig. 1. In Fig. 2(a), we plot over 100 energy distribution curves (EDCs) symmetrized about E_F from 12 to 94 K, measured at k_F of the electron pocket, where false color represents the intensity of the EDCs. In Fig. 2(b), we plot select EDCs extracted from the temperature series in Fig. 2(a). Figure 2(c) tracks Δ as a function of the temperature, defined as half the separation between quasiparticle peaks of the symmetrized EDCs from Figs. 2(a) and 2(b), as well as the evolution of the spectral gap depth δ_{SW}, defined as the difference between the coherence peak amplitude normalized to unity and the corresponding spectral weight at E_F. In Fig. 2(d), we show $R_s(T)$, as well as its derivative dR_s/dT. As the superconducting transition is broad, we define three characteristic temperatures to describe the shape of the transition: T_0, where the resistance reaches 0.1% of $R_s(70\text{ K})$; T_{onset}, the intersection between the extrapolated normal-state sheet resistance and a linear fit to the superconducting transition region; and T^*, where $R_s(T)$ exhibits an inflection point at the onset of the broad resistive rollover (as determined by a local minimum in dR_s/dT). For the sample shown in Fig. 2, $T_0 = 29 \pm 0.2$ K, while $T_{\mathrm{onset}} = 44 \pm 3$ K, and $T^* = 72 \pm 4$ K. Deep within the superconducting state ($T < T_0$), a clear superconducting gap ($\Delta = 12.8 \pm 1$ meV) and sharp Bogoliubov quasiparticle peaks are observed in the ARPES spectra. In the broad transition region where $T_0 < T < T_{\mathrm{onset}}$, the strength of the quasiparticle peak is gradually suppressed as the temperature increases, accompanied by a rapid filling of spectral weight within the gap [Figs. 2(a) and 2(c)], despite the energy separation between the peaks remaining largely constant. Upon

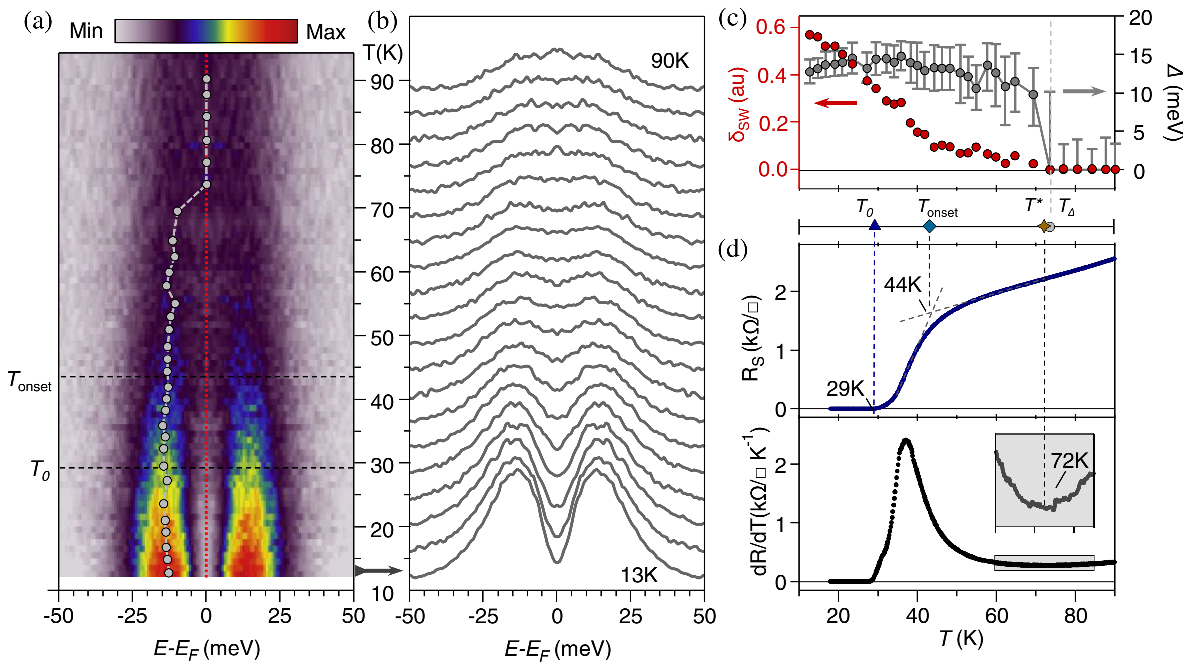

FIG. 2. Comparison of temperature-dependent gap closing behavior and corresponding resistive superconducting transition. (a) Symmetrized EDCs taken at k_F from over 100 individual spectra collected between 12 and 94 K. The color scale indicates the EDC intensity, with increasing temperature along the vertical axis. The gray circles track the quasiparticle peak position as a function of the temperature. (b) Selection of symmetrized EDCs from the data in (a). The temperature (vertical) axis is matched to that of (a). (c) Extracted energy gap Δ (right axis) as a function of the temperature from the data in (a). Δ is defined as half of the separation between the EDC peak positions indicated in (a). The red symbols (left axis) track the suppression spectral weight δ_{SW} at E_F [dotted line in (a)] relative to 90 K. (d) Sheet resistance (blue line, top) and dR/dT (black line, bottom) as a function of the temperature measured *in situ* for the same sample presented in (a) and (b).

increasing the temperature further ($T_{\text{onset}} < T < T^*$), the energy gap continues to fill in at a more gradual rate, until eventually Δ is no longer discernible above $T_\Delta = 73 \pm 5$ K, a temperature that corresponds closely to T^*. We confirm that alternative methods for fitting the symmetrized EDCs to a model spectral function for Bogulibov quasiparticles yields comparable results for T_Δ (Supplemental Material, Sec. III [17]).

This behavior is in stark contrast to what is observed in bulk conventional superconductors, where the resistivity drops abruptly to zero at the same temperature at which the superconducting gap opens (i.e., $T_0 \approx T_{\text{onset}} \equiv T_\Delta$). The most notable exception to this behavior is underdoped cuprates, where the pseudogap at the d-wave antinode measured by numerous techniques including ARPES also opens at significantly higher temperatures than the bulk T_c [18]. In contrast, in bulk Fe-based superconductors, it is widely shown that T_{onset} and T_Δ match closely [19,20], including in electron-doped bulk FeSe-based compounds such as $A_xFe_2Se_2$ ($A = $ K, Cs) and $(Li_{1-x}Fe_x)OHFeSe$ [6,7]. Thus, the observed discrepancy in $FeSe/SrTiO_3$ cannot be solely attributed to the unconventional nature of Fe-based superconductivity. Furthermore, by using spatially resolved ARPES measurements with a 100-μm-diameter beam spot, we observe that Δ is largely uniform across the entire sample, ruling out percolation or spatial variations as the reason for the discrepancy between T_0 and T_{onset} and T_Δ (Appendix B).

On the other hand, such behavior is expected in 2D superconductors which can exhibit a broad Berezinskii-Kosterlitz-Thouless (BKT) transition [21], where vortex-antivortex fluctuations prevent long-range phase coherence at temperatures well above where a zero-resistance state is finally achieved (T_{BKT}). BKT transitions have been extensively studied in disordered 2D superconductors as well as more recently in atomically thin crystalline superconductors or interfaces such as $LaAlO_3/SrTiO_3$ [22] and twisted bilayer graphene [23]. Probes such as ARPES or tunneling spectroscopy detect the initial formation of pairs but are not sensitive to their phase coherence, so a spectroscopic gap can be found to open at temperatures well above a broad resistive transition ($T_\Delta > T_{\text{BKT}}$). Recently, combined tunneling and transport measurements of disordered ultrathin films of the BCS superconductors TiN [24] and NbN [25] have verified such a picture.

To quantitatively investigate the possibility of BKT phase fluctuations in $FeSe/SrTiO_3$, we show $V(I)$ characteristics from the $FeSe/SrTiO_3$ films in Fig. 3 on a log-log scale, measured from 24 to 37 K. The slopes of the curves in Fig. 3(a) indicate the power-law exponent α at low

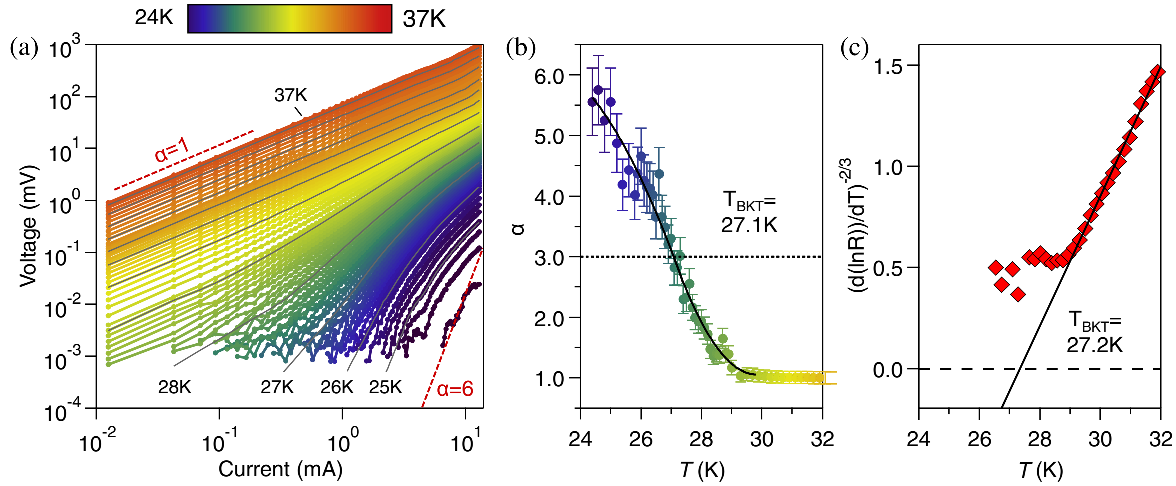

FIG. 3. *In situ* $V(I)$ characteristics and $R(T)$ analysis. (a) Current-voltage characteristics for 1-uc-thick $FeSe/SrTiO_3$, shown on log-log scale. Color indicates the temperature for a given $V - I$ curve, where the gray lines indicate temperature spacings of 1 K. Red dashed lines indicate power-law behavior for $V \propto I^{\alpha}$. (b) Extracted temperature dependence of α from power-law fits to the data in (a). (c) $[d(\ln R)/dT]^{2/3}$ plotted versus T. The solid black line indicates behavior consistent with $T_{\mathrm{BKT}} = 27.2$ K.

voltages for $V(I) \propto I^{\alpha}$ [Fig. 3(b)]. As expected for a BKT-like transition, the values of α are highly temperature dependent, crossing $\alpha = 3$ at $T_{\mathrm{BKT}} = 27.1 \pm 0.5$ K. A plot of $[d(\ln R)/dT]^{2/3}$ [Fig. 3(c)] matching the Halperin-Nelson form of $R_s(T)$ [26] yields a value of $T_{\mathrm{BKT}} = 27.2 \pm 0.5$ K, in agreement with T_{BKT} extracted from the critical exponent analysis. Signatures of a BKT transition are also reported in *ex situ* measurements of capped $FeSe/SrTiO_3$ thin films, albeit with lower values of T_{onset} and T_{BKT} [11].

Since T_0 in 2D superconductors can be strongly influenced by disorder, we systematically investigate a large number of samples with varying degrees of disorder, using the extrapolated residual sheet resistivity R_0 as a metric, and controlled primarily through the postgrowth annealing process [27]. A comparison with ARPES data shows close correspondence between R_0 and increased quasiparticle broadening, consistent with sample-to-sample variation in the disorder strength (Appendix C). At the limit where films become insulating, distinct quasiparticle peaks vanish entirely, and the spectral weight at E_F is strongly suppressed. In Fig. 4(a), we show $R_s(T)$ for a selection of single-layer $FeSe/SrTiO_3$ films, which clearly demonstrates the obvious dependence of T_0 and T_{onset} on R_0. Figure 4(c) summarizes all samples measured in this study, with values of T_0, T_{onset}, T_{Δ}, and T^* extracted from additional samples following the conventions in Fig. 2 (Supplemental Material, Sec. IV [17]). As shown, T_0 decreases linearly with increasing R_0, approaching 40 K in the clean limit. The crossover from a superconducting to insulating regime occurs around $R_0 \approx 7.2$ kΩ, close to the quantum of resistance for pairs, $R_Q = h/(2e)^2$, as would be expected for a 2D superconductor limited by phase fluctuations [28]. The importance of disorder on 2D phase fluctuations naturally explains the wide variation in T_0 and T_{onset} values [2,10–13] previously reported in the literature from capped films [Fig. 4(b)]. The highest values of $T_{\mathrm{onset}} \approx 45$ K reported here on pristine films are slightly higher than the maximum T_{onset} observed in capped films from the literature (approximately 40 K) and are inconsistent with the singular report of $T_c > 100$ K by Ge *et al.* [29].

In contrast to T_0, both T_{Δ} and T^* show relatively little dependence on disorder [Fig. 4(c)], with the values of T_{Δ} reported here generally consistent with the values extracted from the literature using the same analysis method for our own data [Fig. 4(b), gray symbols] [1,3,4,14,30–32]. The close correspondence of T_{Δ} and T^* strongly suggests that the beginning of the resistive transition at T^* is directly related to the appearance of Cooper pairs below T_{Δ}. This incoherent Cooper pairing persists within a high-temperature pseudogap regime ($T_{\mathrm{onset}} < T < T_{\Delta}$) well above the temperature range where 2D BKT-like phase fluctuations are clearly observed ($T < 40$ K).

III. DISCUSSION AND CONCLUSIONS

Taken together, these measurements present, for the first time, a self-consistent picture for the previously mysterious superconducting behavior of $FeSe/SrTiO_3$. At low temperatures ($T < T_0$), the influence of phase fluctuations is minimal, resulting in sharp Bogoliubov quasiparticle peaks and a zero-resistance state. As the temperature is increased, the zero-resistance state is destroyed by a BKT-like vortex-unbinding transition, at a temperature dependent on the level of disorder, while spectral weight begins to fill within the gap. Since T_0 should asymptote to T_c in the clean limit for a 2D superconductor [33], the trend in T_0 demonstrated in Fig. 4(c) suggests that maximum intrinsic T_c of $FeSe/SrTiO_3$ is approximately 40 K, when accounting for disorder and phase fluctuations [Fig. 4(c)], comparable

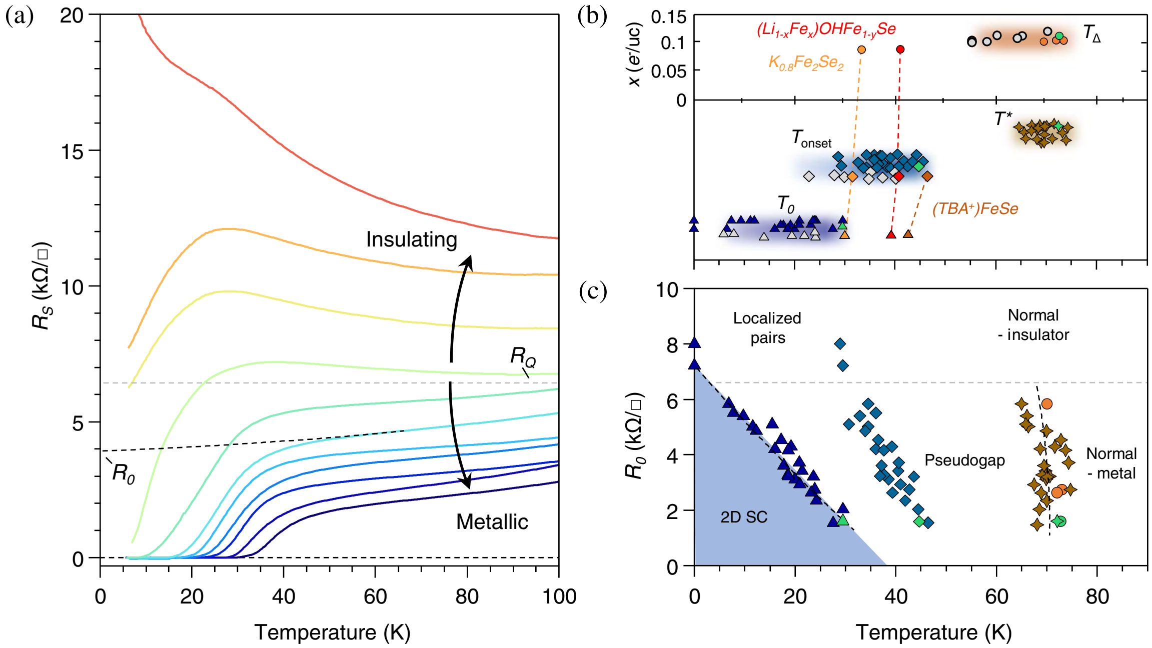

FIG. 4. Disorder-driven superconductor-insulator transition in single-layer $FeSe/SrTiO_3$. (a) R_s for a selection of single-layer $FeSe/SrTiO_3$ films. The residual resistance R_0 for each curve is determined by an extrapolation of the normal state data above T^* (black dashed line). (b) Extracted characteristic temperatures of single-layer $FeSe/SrTiO_3$. Marked symbols indicate T_0 (triangles), T_{onset} (diamonds), T^* (stars), and T_Δ (circles) versus x (Luttinger volume) as measured *in situ* by this study (solid colored symbols) and from the literature (gray filled symbols). T_0, T_{onset}, and T^* values are offset along the Y axis for clarity. Literature data for T_0 and T_{onset} are taken from capped single-layer $FeSe/SrTiO_3$ films. Bright green symbols indicate values for the sample presented in Figs. 1–3. ARPES gap values and doping levels from the literature are reported from Refs. [1,3,4,14,30–32]. *Ex situ* transport data from Refs. [2,10–13]. T_0, T_{onset}, and T_Δ values are also plotted for bulk compounds $K_{0.8}Fe_2Se_2$ (orange, solid line), $(Li_{1-x}Fe_x)OHFeSe$ (red, solid line), and (TBA+)FeSe (brown, solid line). (c) R_0 versus T_0, T_{onset}, T^*, and T_Δ for films measured *in situ* for this work. Extended data for T_Δ and T^* are provided in Supplemental Material, Sec. IV [17].

to typical values of T_c for bulk electron-doped FeSe-based compounds [Fig. 4(b)] such as $(Li_{1-x}Fe_x)OHFeSe$ [7] but well short of the 60–70 K T_c previously interpreted from spectroscopic results alone.

Finally, we speculate on the high-temperature pseudogap regime for $FeSe/SrTiO_3$ ($T_{onset} < T < T_\Delta \approx 60$–70 K), when compared to bulk electron-doped FeSe-based materials which do not exhibit a pseudogap and show $T_\Delta \approx T_c \approx 40$ K. One possibility is that Gaussian fluctuations above T_c account for the behavior observed in the high-temperature pseudogap regime. However, this scenario is contradicted by the observed behavior of $\Delta(T)$, which shows no evidence of closing near 40 K, as well as by the shape of $R_s(T)$, which is poorly reproduced by the Aslamazov-Larkin framework (Supplemental Material, Sec. II [17]). Instead, this behavior suggests that the microscopic, mean-field pairing temperature of $FeSe/SrTiO_3$ is intrinsically higher than that of bulk FeSe-based compounds, even if the ultimate maximum T_c set by the onset of phase coherence (approximately 40 K) for $FeSe/SrTiO_3$ is comparable to those of bulk compounds. Much speculation focuses on the possible influence of interfacial electron-phonon coupling from the $SrTiO_3$ substrate in enhancing the T_c [3,4]. Alternatively, recent work on the highly two-dimensional bulk compound $(TBA^+)FeSe$, where the distance between FeSe layers is expanded to 15.5 Å by intercalation of ion tetrabutyl ammonium organic molecules [compared to 5.5 Å for bulk FeSe or 9.32 Å for $(Li_{1-x}Fe_x)OHFeSe$], also reports evidence of incoherent preformed pairing up to 60 K, comparable to $FeSe/SrTiO_3$, but in the absence of any substrate [34]. That similar pseudogap features are also observed in the more two-dimensional $(TBA^+)FeSe$ suggests that the increased two-dimensional nature of the electronic or crystal structure could potentially be the origin of the enhanced mean-field pairing temperature T_Δ in $FeSe/SrTiO_3$. While it is empirically known that a two-dimensional electronic structure appears to be a key ingredient for unconventional high-temperature superconductivity (e.g., cuprates, Fe-based superconductors, and nickelates), most Fe-based superconductors exhibit some degree of three-dimensionality in their electronic structure, as evidenced by k_z dispersion in ARPES [35], as well as their resistivity anisotropy ρ_c/ρ_{ab} being in the range of 2–3 for the 11 and 111 families or up to 10^2 for the 122 compounds [36–38]. This behavior is in contrast to their more two-dimensional, higher T_c cuprate analogues such as $Bi_2Sr_2CaCu_2O_{8+\delta}$, $YBa_2Cu_3O_{7-\delta}$, or $La_{2-x}Sr_xCuO_4$,

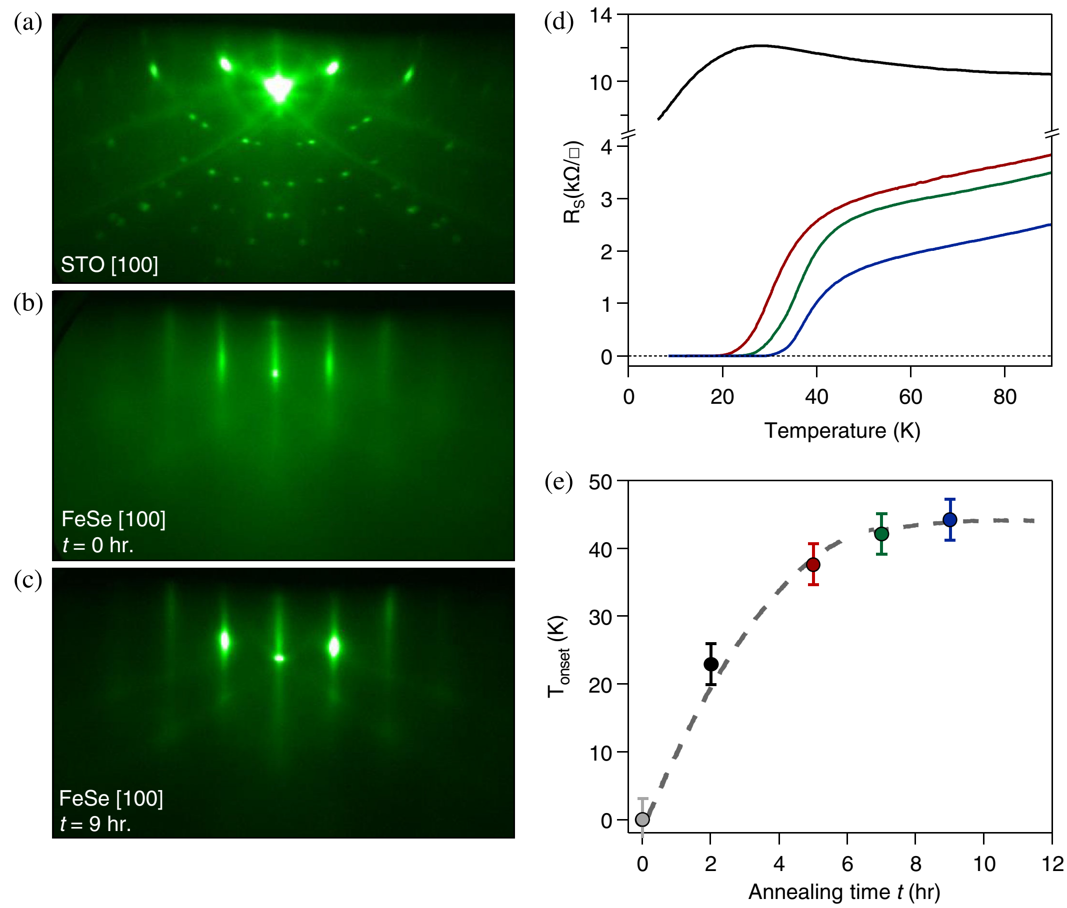

FIG. 5. RHEED images along the crystallographic [100] direction for (a) $SrTiO_3$ substrate prior to film deposition, (b) single-layer FeSe film immediately after growth, and (c) single-layer FeSe upon reaching maximum T_c following 9 h accumulated annealing time at 450 °C. (d) *In situ* resistivity data as a function of accumulated annealing time t. (e) T_{onset} as a function of cumulative annealing time t.

where ρ_c/ρ_{ab} is much larger, in the range of 10^3–10^6 [39]. By pushing Fe-based superconductors closer to the idealized two-dimensional limit as in (TBA+)FeSe ($\rho_c/\rho_{ab} \approx 10^5$) or in the ultimate case of single-layer $FeSe/SrTiO_3$, it is possible that the strength of the microscopic pairing is increased but at the cost of 2D phase fluctuations and enhanced sensitivity to disorder which limit T_0.

IV. METHODS

Single-layer $FeSe/SrTiO_3$ films are synthesized on $SrTiO_3$ (001) substrates using a chalcogenide molecular beam epitaxy system as reported previously [3]. Se (99.999% purity) and Fe (99.995% purity) are coevaporated at a nominal flux ratio of 5∶1 and at a nominal growth rate of 1.8–2 unit cells (uc) per minute, with source fluxes calibrated by a quartz crystal monitor and film crystallinity monitored in real time using reflection high-energy electron diffraction [RHEED, Figs. 5(a)–5(c)]. To enable reliable resistivity measurements of the FeSe monolayer, we utilize undoped insulating $SrTiO_3$ for all films presented in this work. After growth films are progressively annealed until optimal superconducting properties are achieved [Figs. 5(d) and 5(e)], followed by deposition of 20-nm-thick Au electrodes at the sample corners using a shadow mask to provide reliable four-point electrical contact (Fig. S3 [17]).

In situ resistivity measurements are performed using a custom-built UHV four-point transport probe with a base temperature of 5.2 K and a base pressure of 7×10^{-11} Torr. Contact is applied directly to the film using a set of Au-plated spring-loaded probes in a van der Pauw geometry, with a nominal instrumental contact spacing of 7 mm. Resistance measurements are taken using a Keithley 6221/2182A current source–voltmeter combination in delta mode (Fig. S2 [17]) with a typical applied current of $1-10$ μA.

ARPES measurements are taken with a VG Scienta R4000 electron analyzer equipped with a VUV5000 helium discharge lamp using He-I photons at 21.2 eV. The base pressure in the ARPES system is 5×10^{-11} Torr. The energy resolution is nominally set at 12 meV for mapping and 9 meV for gap measurements. To avoid sample charging during ARPES measurement, the film is grounded using a retractable contact pin built onto the sample manipulator [Fig. S3(a) [17]]. For gap measurements, the Fermi level is referenced to the measured Fermi edge of the Au electrodes [Fig. S3(c) [17]].

ACKNOWLEDGMENTS

We thank P. B. Littlewood for helpful discussions and E. Rotenberg, C. Jozwiak, and A. Bostwick for assistance in the spatially resolved ARPES measurements in Fig. 6. This work was primarily supported through the Air Force Office of Scientific Research Grants No. FA9550-15-1-0474 and No. FA9550-21-1-0168. This work was also supported through the National Science Foundation Platform for the Accelerated Realization, Analysis, and Discovery of Interface Materials (PARADIM) under Cooperative Agreement No. DMR-1539918, National Science Foundation (NSF) No. DMR-1709255, and the Gordon and Betty Moore Foundation's EPiQS Initiative through Grant No. GBMF3850 to Cornell University. B. D. F. and J. N. N. acknowledge support from the NSF Graduate Research Fellowship under Grant No. DGE-1650441. P. M. acknowledges support from the Indo U.S. Science and Technology Forum (IUSSTF). This work made use of the Cornell Center for Materials Research (CCMR) Shared Facilities, which are supported through the NSF MRSEC Program (No. DMR-1719875). Substrate preparation was performed in part at the Cornell NanoScale Facility, a member of the National Nanotechnology Coordinated Infrastructure (NNCI), which is supported by the NSF (Grant No. ECCS-1542081).

APPENDIX A: FILM SYNTHESIS AND OPTIMIZATION OF SUPERCONDUCTING PROPERTIES

An additional postgrowth annealing step is known to be critical for producing superconductivity in ultrathin $FeSe/SrTiO_3$ films. This postgrowth annealing serves several purposes. First, it removes excess Se from the film present due to the adsorption-control growth regime, improving the stoichiometry [40,41]. Superconductivity in both FeSe films and crystals is known to be highly sensitive to nonstoichiometry [42]. Additionally, the annealing reduces disorder in the form of Fe-vacancy defects [27], increasing the electron mean free path and reducing the sheet resistance, macroscopically.

In Fig. 5, we present RHEED and *in situ* transport characteristics for a representative single-layer $FeSe/SrTiO_3$ film both before growth and afterward as it is progressively annealed to achieve optimal superconducting properties. Prior to film growth, undoped $SrTiO_3$ substrates (10 mm × 10 mm, Shinkosha) are annealed at 600 °C for 3 h and then cooled to 420 °C for deposition. $SrTiO_3$ substrates prepared in this fashion typically exhibit a clear $\sqrt{13} \times \sqrt{13}$ surface reconstruction, indicating the presence of a TiO_2 double-layer structure at the substrate surface [12,43]. Upon initial growth, the film exhibits weak RHEED spots and strongly insulating low-temperature transport behavior. With progressive annealing at 450 °C postgrowth, the film eventually becomes metallic and superconducting, reaching an optimal T_c (in this case) after 9 h. The RHEED pattern for

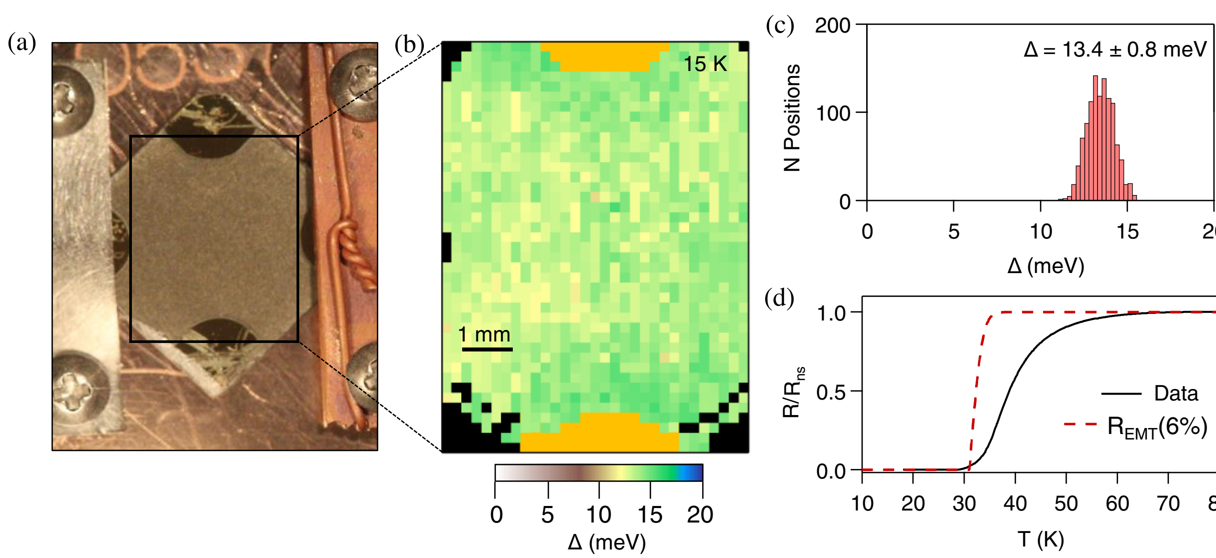

FIG. 6. Spatially resolved ARPES measurements of the superconducting gap. (a) Camera image of the single-layer $FeSe/SrTiO_3$ sample as mounted for beam line ARPES measurements. (b) Spatially resolved gap distribution measured across the sample surface of the region indicated in (a). The region probed is 8 mm × 6 mm. The gold-colored regions indicate areas with Au electrodes, and the black indicate regions where no FeSe signal is observed. (c) Histogram showing the statistical distribution of Δ_e from the data in (b). The local gap values form a Gaussian-like distribution with a mean of 13.4 meV and a standard deviation of 0.8 meV. (d) $R(T)$ data normalized to the extrapolated normal state resistance (black line) compared to expected behavior for a percolative superconducting transition (dashed red line) assuming a local T_c distribution matching the data in (c).

optimally annealed films shows sharp, well-defined spots and distinct Kikuchi lines, indicating an atomically flat surface with improved crystallinity. This behavior is consistently observed across all films prepared for this study, although the optimal annealing time is found to vary somewhat across films, falling within the range of 5–12 h typically.

APPENDIX B: EVALUATION OF INHOMOGENEITY EFFECTS

Because our measurements probe a macroscopic average of the film, the discrepancy in transport and ARPES results as well as the broad resistive transitions could conceivably be explained by gross sample inhomogeneity. To rule this possibility out, we perform spatially resolved measurements of the same single-layer $FeSe/SrTiO_3$ sample presented in Figs. 1–3, transported under vacuum to beam line 7.0.2 (MAESTRO) of the Advanced Light Source at Lawrence Berkeley National Laboratory. For beam line ARPES measurements, we set the photon energy and polarization to 24 eV and p polarization, respectively, and fix the beam diameter to a 100-μm spot for spatially resolved measurements. Figure 6(b) shows the spatially resolved distribution of Δ across an 8 mm × 6 mm region of the film, as measured at 15 K. All regions of the film show single-layer FeSe band structure, except for the

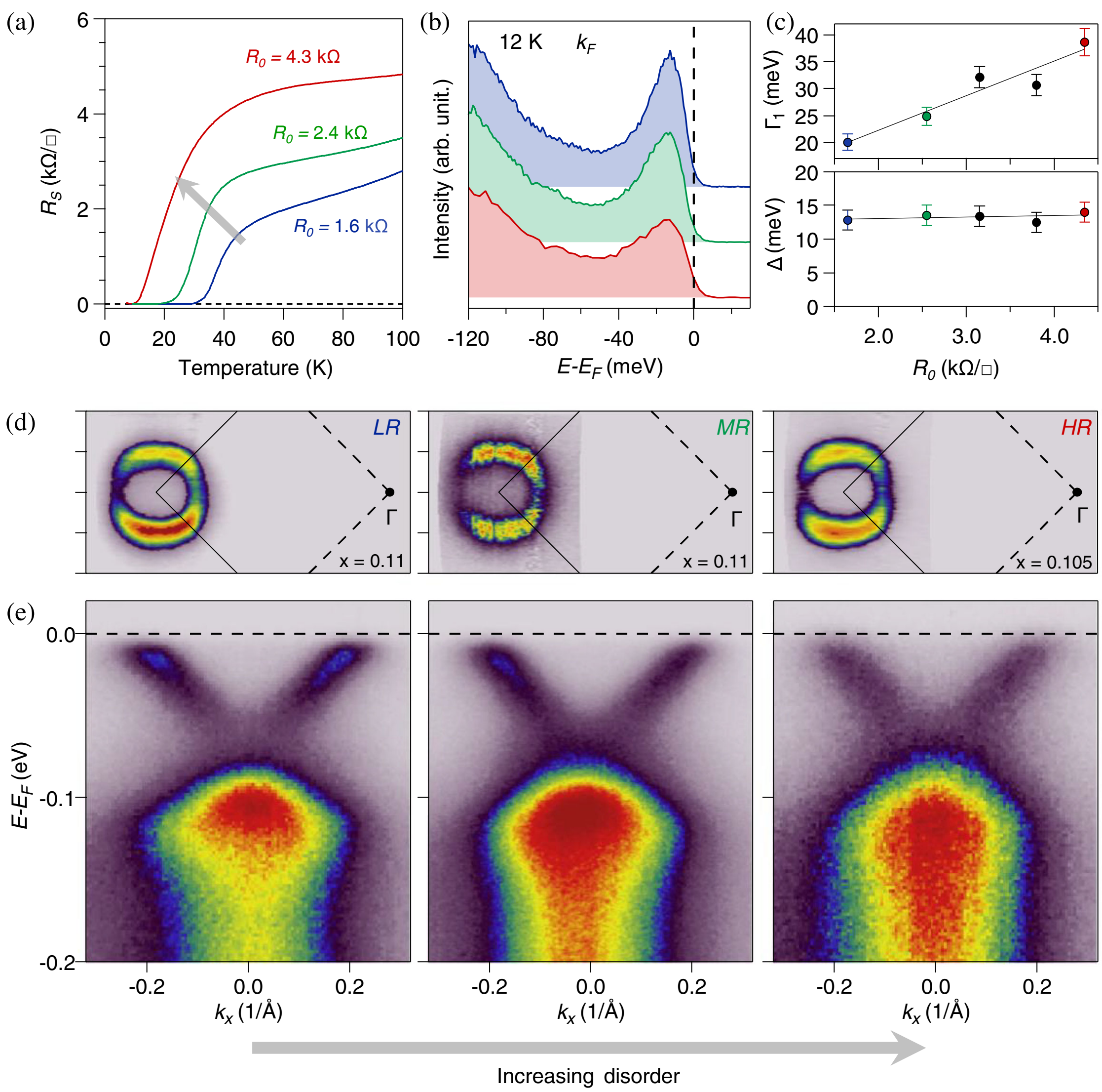

FIG. 7. Comparison of the resistive transition and ARPES band structure for films at different annealing conditions. (a) *In situ* $R_s(T)$ measurements show that the onset of zero resistance is suppressed to lower temperatures in more resistive films. (b) Comparison of raw EDCs at k_F for the same films measured in (a). (c) Comparison of quasiparticle half-width Γ_1 (top) and Δ (bottom) against residual resistance R_0. Black markers indicate data for samples also measured by ARPES and *in situ* resistivity at low temperature but not presented in (a),(b). (d) Fermi surface maps and (e) high statistics cuts at M, showing minimal variation in the doping content x based on Luttinger volume.

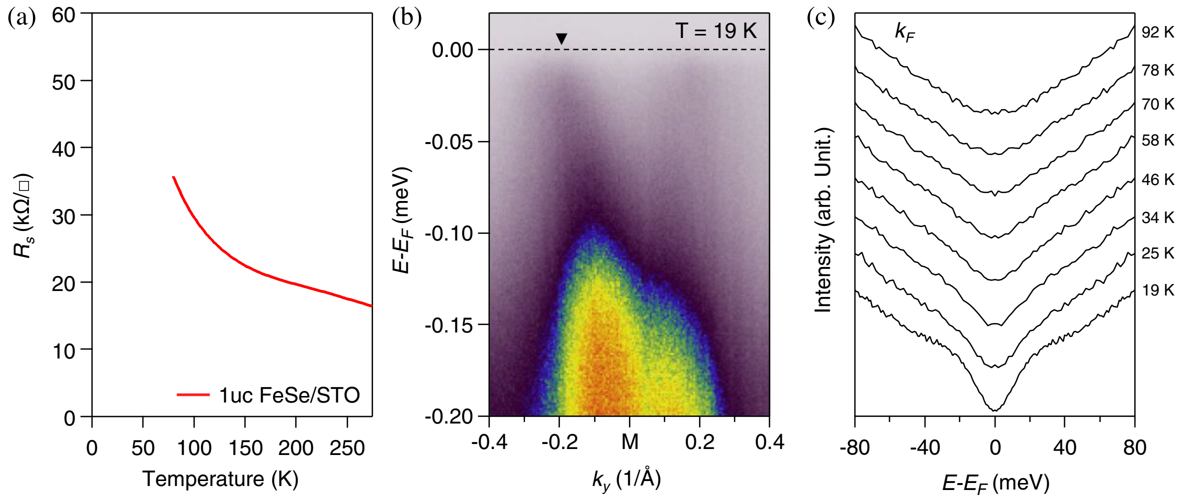

FIG. 8. ARPES behavior of insulating single-layer FeSe/$SrTiO_3$. (a) *In situ* $R_s(T)$ data for an insulating single-layer FeSe/$SrTiO_3$ film. (b) ARPES spectra taken at M at $T = 19$ K. (c) Temperature-dependent symmetrized EDCs at k_F as indicated by the arrow in (b).

corners which host Au electrodes. In particular, we observe no multilayer band structure or void regions. Therefore, we conclude that the film is indeed a macroscopically homogeneous monolayer. The measurable variation in superconducting gap at 15 K follows a normal distribution, with $\Delta = 13.4$ meV and $\sigma_\Delta = 0.82$ meV [Fig. 6(c)]. We observe no FeSe regions over which a superconducting gap is not present.

To show that this level of inhomogeneity cannot account for our broad resistive transition, in Fig. 6(d) we simulate the expected behavior of $R(T)$, assuming a percolative network with a T_c distribution matching the ARPES gap data from Fig. 6(a), based on the predictions of effective medium theory [44]. The simulated transition (red dashed curve) is far too narrow to account for the broadness of the transition that we observe by *in situ* measurement (solid black curve). Therefore, spatial inhomogeneities cannot explain the discrepancy between the temperature dependence of the superconducting gap by ARPES and our electrical resistivity measurements.

APPENDIX C: INFLUENCE OF DISORDER AND DOPING VARIATION ON ARPES AND TRANSPORT BEHAVIOR

The wide variation in T_0 observed across samples raises natural questions about what drives the suppression of superconductivity in monolayer FeSe/$SrTiO_3$ films. One possibility is that natural variation in the interfacial charge transfer from the $SrTiO_3$ interface leads to variation in the electron doping x across samples. To rule out this scenario, in Fig. 7 we compare ARPES and transport behavior across a series of films with substantially different values of T_0. Figure 7(a) shows low-temperature $R_s(T)$ behavior for three separate samples labeled as LR (low-resistance), MR (medium-resistance), and HR (high-resistance), with T_0's that span the observed range for superconducting films presented in Fig. 4(c). LR is identical to the sample presented in Figs. 1–3 of the main text. The residual resistance R_0 in each case is determined by extrapolating the high-temperature $R(T)$ behavior to 0 K and is found to be 1.6, 2.4, and 4.3 kΩ for samples LR, MR, and HR, respectively. Figure 7(b) shows corresponding EDCs at k_F extracted from the ARPES spectra on the same samples [Fig. 7(e)], and Fig. 7(c) tracks the extracted scattering rate Γ_1 (top) and low-temperature gap magnitude (bottom) versus R_0 for all films for which ARPES and *in situ* transport data are available. Despite the substantial variation in T_0, both the gap magnitude [Fig. 7(c)] and doping level (as deduced from the Luttinger volume [Fig. 7(d)]) are highly consistent across films, ruling out irregular charge transfer as the cause of the variation in the resistive behavior.

Figure 8 shows combined *in situ* resistivity and ARPES data for an even more disordered single-layer FeSe/$SrTiO_3$ film, which is “insulating” (negative dR/dT) at low temperatures [Fig. 8(a)]. The main difference between this sample and the superconducting samples is the lack of distinct quasiparticle peaks, coincident with a significant suppression of the weight near E_F [Fig. 8(c)].

[1] D. Liu, W. Zhang, D. Mou, J. He, Y. Ou, Q.-Y. Wang, Z. Li, L. Wang, L. Zhao, S. He, Y. Peng, X. Liu, C. Chen, L. Yu, G. Liu, X. Dong, J. Zhang, C. Chen, Z. Xu, and X. J. Zhou, *Electronic Origin of High Temperature Superconductivity in Single-Layer FeSe Superconductor*, Nat. Commun. **3**, 931 (2012).

[2] M. Yang, C. Yan, Y. Ma, L. Li, and C. Cen, *Light Induced Non-Volatile Switching of Superconductivity in Single Layer FeSe on* $SrTiO_3$ *Substrate*, Nat. Commun. **10**, 85 (2019).

[3] J. J. Lee, F. T. Schmitt, R. G. Moore, S. Johnston, Y.-T. Cui, W. Li, M. Yi, Z. K. Liu, M. Hashimoto, Y. Zhang, D. H. Lu, T. P. Devereaux, D.-H. Lee, and Z.-X. Shen, *Interfacial Mode Coupling as the Origin of the Enhancement of* T_c *in FeSe Films on* $SrTiO_3$, Nature (London) **515**, 245 (2014).

[4] Q. Song, T. L. Yu, X. Lou, B. P. Xie, H. C. Xu, C. H. P. Wen, Q. Yao, S. Y. Zhang, X. T. Zhu, J. D. Guo, R. Peng, and D. L. Feng, *Evidence of Cooperative Effect on the Enhanced Superconducting Transition Temperature at the* $FeSe/SrTiO_3$ *Interface*, Nat. Commun. **10**, 758 (2019).

[5] F.-C. Hsu, J.-Y. Luo, K.-W. Yeh, T.-K. Chen, T.-W. Huang, P. M. Wu, Y.-C. Lee, Y.-L. Huang, Y.-Y. Chu, D.-C. Yan, and M.-K. Wu, *Superconductivity in the PbO-type Structure* α-FeSe, Proc. Natl. Acad. Sci. U.S.A. **105**, 14262 (2008).

[6] L. Zhao *et al.*, *Common Electronic Origin of Superconductivity in (Li,Fe)OHFeSe Bulk Superconductor and Single-Layer* $FeSe/SrTiO_3$ *Films*, Nat. Commun. **7**, 10608 (2016).

[7] Y. Zhang, L. X. Yang, M. Xu, Z. R. Ye, F. Chen, C. He, H. C. Xu, J. Jiang, B. P. Xie, J. J. Ying, X. F. Wang, X. H. Chen, J. P. Hu, M. Matsunami, S. Kimura, and D. L. Feng, *Nodeless Superconducting Gap in* $A_xFe_2Se_2$ $(A = K, Cs)$ *Revealed by Angle-Resolved Photoemission Spectroscopy*, Nat. Mater. **10**, 273 (2011).

[8] Y. Xing and J. Wang, *Direct Evidence of High Temperature Superconductivity in one-unit-cell FeSe Films on* $SrTiO_3$ *Substrate by Transport and Magnetization Measurements*, Chin. Phys. B **24**, 117404 (2015).

[9] S. He *et al.*, *Phase Diagram and Electronic Indication of High-Temperature Superconductivity at 65 K in Single-Layer FeSe Films*, Nat. Mater. **12**, 605 (2013).

[10] Wen-Hao Zhang *et al.*, *Direct Observation of High-Temperature Superconductivity in One-Unit-Cell FeSe Films*, Chin. Phys. Lett. **31**, 017401 (2014).

[11] W. Zhao, C.-Z. Chang, X. Xi, K. F. Mak, and J. S. Moodera, *Vortex Phase Transitions in Monolayer FeSe Film on* $SrTiO_3$, 2D Mater. **3**, 024006 (2016).

[12] W. Zhao, M. Li, C.-Z. Chang, J. Jiang, L. Wu, C. Liu, J. S. Moodera, Y. Zhu, and M. H. W. Chan, *Direct Imaging of Electron Transfer and Its Influence on Superconducting Pairing at* $FeSe/SrTiO_3$ *Interface*, Sci. Adv. **4**, eaao2682 (2018).

[13] Q. Wang, W. Zhang, W. Chen, Y. Xing, Y. Sun, Z. Wang, J.-W. Mei, Z. Wang, L. Wang, X.-C. Ma, F. Liu, Q.-K. Xue, and J. Wang, *Spin Fluctuation Induced Linear Magnetoresistance in Ultrathin Superconducting FeSe Films*, 2D Mater. **4**, 034004 (2017).

[14] S. Tan, Y. Zhang, M. Xia, Z. Ye, F. Chen, X. Xie, R. Peng, D. Xu, Q. Fan, H. Xu, J. Jiang, T. Zhang, X. Lai, T. Xiang, J. Hu, B. Xie, and D. Feng, *Interface-Induced Superconductivity and Strain-Dependent Spin Density Waves in* $FeSe/SrTiO_3$ *Thin Films*, Nat. Mater. **12**, 634 (2013).

[15] Y. Zhang, J. J. Lee, R. G. Moore, W. Li, M. Yi, M. Hashimoto, D. H. Lu, T. P. Devereaux, D.-H. Lee, and Z.-X. Shen, *Superconducting Gap Anisotropy in Monolayer FeSe Thin Film*, Phys. Rev. Lett. **117**, 117001 (2016).

[16] J. P. Sun, P. Shahi, H. X. Zhou, Y. L. Huang, K. Y. Chen, B. S. Wang, S. L. Ni, N. N. Li, K. Zhang, W. G. Yang, Y. Uwatoko, G. Xing, J. Sun, D. J. Singh, K. Jin, F. Zhou, G. M. Zhang, X. L. Dong, Z. X. Zhao, and J.-G. Cheng, *Reemergence of High-*T_c *Superconductivity in* $(Li_{1-x}Fe_x)OHFe_{1-y}Se$ *Under High Pressure*, Nat. Commun. **9**, 380 (2018).

[17] See Supplemental Material at http://link.aps.org/supplemental/10.1103/PhysRevX.11.021054 for details on the evaluation of *in situ* contact resistance and determination of R_s, fitting of the superconducting transition to theoretical models, measurement and evaluation of the superconducting gap, and data from additional samples.

[18] A. G. Loeser, Z.-X. Shen, D. S. Dessau, D. S. Marshall, C. H. Park, P. Fournier, and A. Kapitulnik, *Excitation Gap in the Normal State of Underdoped* $Bi_2Sr_2CaCu_2O_8$, Science **273**, 325 (1996).

[19] H. Ding, P. Richard, K. Nakayama, K. Sugawara, T. Arakane, Y. Sekiba, A. Takayama, S. Souma, T. Sato, T. Takahashi, Z. Wang, X. Dai, Z. Fang, G. F. Chen, J. L. Luo, and N. L. Wang, *Observation of Fermi-Surface–Dependent Nodeless Superconducting Gaps in* $Ba_{0.6}K_{0.4}Fe_2As_2$, Europhys. Lett. **83**, 47001 (2008).

[20] G. R. Stewart, *Superconductivity in Iron Compounds*, Rev. Mod. Phys. **83**, 1589 (2011).

[21] J. M. Kosterlitz and D. J. Thouless, *Ordering, Metastability and Phase Transitions in Two-Dimensional Systems*, J. Phys. C **6**, 1181 (1973).

[22] N. Reyren, S. Thiel, A. D. Caviglia, L. F. Kourkoutis, G. Hammerl, C. Richter, C. W. Schneider, T. Kopp, A.-S. Rüetschi, D. Jaccard, M. Gabay, D. A. Muller, J.-M. Triscone, and J. Mannhart, *Superconducting Interfaces between Insulating Oxides*, Science **317**, 1196 (2007).

[23] Y. Cao, V. Fatemi, S. Fang, K. Watanabe, T. Taniguchi, E. Kaxiras, and P. Jarillo-Herrero, *Unconventional Superconductivity in Magic-Angle Graphene Superlattices*, Nature (London) **556**, 43 (2018).

[24] B. Sacépé, C. Chapelier, T. I. Baturina, V. M. Vinokur, M. R. Baklanov, and M. Sanquer, *Pseudogap in a Thin Film of a Conventional Superconductor*, Nat. Commun. **1**, 140 (2010).

[25] M. Mondal, A. Kamlapure, M. Chand, G. Saraswat, S. Kumar, J. Jesudasan, L. Benfatto, V. Tripathi, and P. Raychaudhuri, *Phase Fluctuations in a Strongly Disordered s-Wave NbN Superconductor Close to the Metal-Insulator Transition*, Phys. Rev. Lett. **106**, 047001 (2011).

[26] B. I. Halperin and D. R. Nelson, *Resistive Transition in Superconducting Films*, J. Low Temp. Phys. **36**, 599 (1979).

[27] D. Huang, T. A. Webb, C.-L. Song, C.-Z. Chang, J. S. Moodera, E. Kaxiras, and J. E. Hoffman, *Dumbbell Defects in FeSe Films: A Scanning Tunneling Microscopy and First-Principles Investigation*, Nano Lett. **16**, 4224 (2016).

[28] M. P. A. Fisher, G. Grinstein, and S. M. Girvin, *Presence of Quantum Diffusion in Two Dimensions: Universal Resistance at the Superconductor-Insulator Transition*, Phys. Rev. Lett. **64**, 587 (1990).

[29] J.-F. Ge, Z.-L. Liu, C. Liu, C.-L. Gao, D. Qian, Q.-K. Xue, Y. Liu, and J.-F. Jia, *Superconductivity above 100 K in Single-Layer FeSe Films on Doped* $SrTiO_3$, Nat. Mater. **14**, 285 (2015).

[30] J. He *et al.*, *Electronic Evidence of an Insulator-Superconductor Crossover in Single-Layer* $FeSe/SrTiO_3$ *Films*, Proc. Natl. Acad. Sci. U.S.A. **111**, 18501 (2014).

[31] R. Peng, X. P. Shen, X. Xie, H. C. Xu, S. Y. Tan, M. Xia, T. Zhang, H. Y. Cao, X. G. Gong, J. P. Hu, B. P. Xie, and D. L. Feng, *Measurement of an Enhanced Superconducting*

Phase and a Pronounced Anisotropy of the Energy Gap of a Strained FeSe Single Layer in FeSe/Nb:$SrTiO_3$/$KTaO_3$ *Heterostructures Using Photoemission Spectroscopy*, Phys. Rev. Lett. **112**, 107001 (2014).

[32] R. Peng, H. C. Xu, S. Y. Tan, H. Y. Cao, M. Xia, X. P. Shen, Z. C. Huang, C. H. P. Wen, Q. Song, T. Zhang, B. P. Xie, X. G. Gong, and D. L. Feng, *Tuning the Band Structure and Superconductivity in Single-Layer FeSe by Interface Engineering*, Nat. Commun. **5**, 5044 (2014).

[33] M. R. Beasley, J. E. Mooij, and T. P. Orlando, *Possibility of Vortex-Antivortex Pair Dissociation in Two-Dimensional Superconductors*, Phys. Rev. Lett. **42**, 1165 (1979).

[34] B. L. Kang, M. Z. Shi, S. J. Li, H. H. Wang, Q. Zhang, D. Zhao, J. Li, D. W. Song, L. X. Zheng, L. P. Nie, T. Wu, and X. H. Chen, *Preformed Cooper Pairs in Layered FeSe-Based Superconductors*, Phys. Rev. Lett. **125**, 097003 (2020).

[35] C. Liu, T. Kondo, N. Ni, A. D. Palczewski, A. Bostwick, G. D. Samolyuk, R. Khasanov, M. Shi, E. Rotenberg, S. L. Bud'ko, P. C. Canfield, and A. Kaminski, *Three- to Two-Dimensional Transition of the Electronic Structure in* $CaFe_2As_2$*: A Parent Compound for an Iron Arsenic High-Temperature Superconductor*, Phys. Rev. Lett. **102**, 167004 (2009).

[36] S. I. Vedeneev, B. A. Piot, D. K. Maude, and A. V. Sadakov, *Temperature Dependence of the Upper Critical Field of FeSe Single Crystals*, Phys. Rev. B **87**, 134512 (2013).

[37] Y. J. Song, J. S. Ghim, B. H. Min, Y. S. Kwon, M. H. Jung, and J.-S. Rhyee, *Synthesis, Anisotropy, and Superconducting Properties of LiFeAs Single Crystal*, Appl. Phys. Lett. **96**, 212508 (2010).

[38] G. F. Chen, Z. Li, J. Dong, G. Li, W. Z. Hu, X. D. Zhang, X. H. Song, P. Zheng, N. L. Wang, and J. L. Luo, *Transport and Anisotropy in Single-Crystalline* $SrFe_2As_2$ *and* $A_{0.6}K_{0.4}Fe_2As_2$ *(A = Sr, Ba) Superconductors*, Phys. Rev. B **78**, 224512 (2008).

[39] S. Komiya, Y. Ando, X. F. Sun, and A. N. Lavrov, *c-Axis Transport and Resistivity Anisotropy of Lightly to Moderately Doped* $La_{2-x}Sr_xCuO_4$ *Single Crystals: Implications on the Charge Transport Mechanism*, Phys. Rev. B **65**, 214535 (2002).

[40] C. Liu and K. Zou, *Tuning Stoichiometry and its Impact on Superconductivity of Monolayer and Multilayer FeSe on* $SrTiO_3$, Phys. Rev. B **101**, 140502(R) (2020).

[41] F. Li, Q. Zhang, C. Tang, C. Liu, J. Shi, C. Nie, G. Zhou, Z. Li, W. Zhang, C.-L. Song, K. He, S. Ji, S. Zhang, L. Gu, L. Wang, X.-C. Ma, and Q.-K. Xue, *Atomically Resolved* FeSe/$SrTiO_3$(001) *Interface Structure by Scanning Transmission Electron Microscopy*, 2D Mater. **3**, 024002 (2016).

[42] T. M. McQueen, Q. Huang, V. Ksenofontov, C. Felser, Q. Xu, H. Zandbergen, Y. S. Hor, J. Allred, A. J. Williams, D. Qu, J. Checkelsky, N. P. Ong, and R. J. Cava, *Extreme Sensitivity of Superconductivity to Stoichiometry in* $Fe_{1+\delta}Se$, Phys. Rev. B **79**, 014522 (2009).

[43] K. Zou, S. Mandal, S. D. Albright, R. Peng, Y. Pu, D. Kumah, C. Lau, G. H. Simon, O. E. Dagdeviren, X. He, I. Božović, U. D. Schwarz, E. I. Altman, D. Feng, F. J. Walker, S. Ismail-Beigi, and C. H. Ahn, *Role of Double* TiO_2 *Layers at the Interface of* FeSe/$SrTiO_3$ *Superconductors*, Phys. Rev. B **93**, 180506(R) (2016).

[44] S. Caprara, M. Grilli, L. Benfatto, and C. Castellani, *Effective Medium Theory for Superconducting Layers: A Systematic Analysis Including Space Correlation Effects*, Phys. Rev. B **84**, 014514 (2011).

Incoherent Cooper pairing and pseudogap behavior in single-layer FeSe/$SrTiO_3$- SUPPLEMENTAL INFORMATION

B.D. Faeth,[1] S.-L. Yang,[1,2,3] J.K. Kawasaki,[1] J.N. Nelson,[1] P. Mishra,[1] C.T. Parzyck,[1] C. Li,[1] D.G. Schlom,[3] and K.M. Shen[1,2]

[1]*Department of Physics, Laboratory of Atomic and Solid State Physics, Cornell University, Ithaca, New York 14853, USA*
[2]*Kavli Institute at Cornell for Nanoscale Science, Ithaca, NY 14853, USA*
[3]*Department of Materials Science and Engineering, Cornell University, Ithaca, NY 14853, USA*

(Dated: April 16, 2021)

I. EVALUATION OF *IN SITU* CONTACT RESISTANCE AND DETERMINATION OF R_s

To ensure that our *in situ* resistivity measurements are not influenced by loss of electrical contact with the monolayer films, we simultaneously measure 2-point electrical resistances across all available lead pairs during 4-point $R(T)$ measurement using a Keithley 3706 matrix relay board. Figure S1 shows comprehensive 2 and 4-point $R(T)$ and $V(I)$ characteristics for a representative single-layer FeSe/$SrTiO_3$ film as measured through the superconducting transition. Within this range of applied current values ($|I| \leq 50\ \mu$A, well below I_c) the $V(I)$ curves remain linear for all measured pairs both below and above the onset of zero resistance at T_0, indicating reliable ohmic contact. For $T < T_0$, 2-point resistances are measured to be $\approx 100\ \Omega$ [Fig. S1(b)], implying typical contact resistances in the range of $\approx 50\ \Omega$ per probe. Additionally, the resistance to ground across all contacts are checked and confirmed to remain open throughout measurements. Together, this characterization ensures that our *in situ* transport measurements reflect the intrinsic behavior of only the isolated single layer FeSe.

Some anisotropy is present in the shape of the resistive transitions for the perpendicular 4-point configurations $I_{13}V_{24}$ versus $I_{12}V_{34}$, as shown in Figure S1(a). As monolayer FeSe/$SrTiO_3$ remains epitaxially locked into the tetragonal phase down to low temperature, we speculate that anisotropy may be instead due to the relative orientation of the current direction compared to the $SrTiO_3$ step edges, which can act as scattering planes. Similar behavior has been previously reported for for ($\sqrt{7} \times \sqrt{3}$)-In surface reconstructions on Si(111) [1] as well as in ultra-thin metallic Ga [2]. To minimize the influence of such an effect on our results, sheet resistance values reported here are calculated using the preferred (lower resistance) direction such that:

$$R_s = \frac{1.34\pi}{\ln(2)} \frac{V_{24}}{I_{13}}, \tag{1}$$

where $\frac{\pi}{\ln(2)}$ is the Van der Pauw factor and 1.34 is an additional factor to account for the finite contact dimensions based on the known dimensions of the Au electrodes [3]. For films measured without gold electrodes present, we instead use a correction factor of 1.1, based on a finite-element analysis of the Van der Pauw correction factor for our known probe geometry.

For $V(I)$ measurement, to minimize potential sample heating effects, a pulse-current measurement mode with a low duty cycle (0.2%) is utilized. In this mode the measurement current is applied in short duration pulses separated in time by some pulse interval, as shown in Fig. S2(a). Prior to final measurement, current pulse settings are calibrated by sweeping the pulse interval and width [Fig. S2(b,c)], and selecting pulse parameters such that the nonlinear deviation at high current is minimized. For the data shown in Figure 3, we use a pulse width of 1 ms with an interval of 500 ms, where the pulse amplitude is stepped from 1 uA to an instrumentally limited value of 10 mA.

II. FITTING OF THE SUPERCONDUCTING TRANSITION TO THE BEREZINSKII-KOSTERLITZ-THOULESS AND AZLAMAZOV-LARKIN MODELS

Two-dimensional superconductors exhibit a complicated critical phenomenology compared to the conventional 3D case; in the following section we consider the underlying mechanism of 2D phase fluctuations and its implications on the transport and ARPES behavior we observe in single-layer FeSe/$SrTiO_3$ films.

In the 2D limit the long-range correlation of the superconducting order parameter is famously prohibited by the Mermin-Wagner theorem [4]; instead 2D superconductors exhibit a Berezinskii-Kosterlitz-Thouless (BKT) type phase transition [5], which allows for the establishment of a quasi-long-range order only at some T_{BKT} below the mean-field pairing temperature T_c. The 2D BKT superconducting state is characterized by the binding of vortex-antivortex pairs (vortices with opposite supercurrent circulation). Whereas unpinned free vortexes produce energy dissipation (and thus a finite resistance) as a result of flux flow (as in a conventional type-II superconductor), bound vortex pairs experience no net Lorentz force from a transport current, and thus allow for dissipation-free transport. Below the critical temperature T_{BKT}, the thermal energy is insufficient to break bound antiparallel vortex pairs, and thus the system will exhibit zero electrical resistance in the absence of external perturbation. A finite applied current will disassociate vortex pairs, generating free vortices and subsequently a voltage response in the form of:

$$V \propto I^{\alpha(T)}, \quad T < T_{BKT}, \tag{2}$$

where $\alpha(T)$ is proportional to the number of unbound vortices times the drift rate across the current. Just at the transition point this is predicted to result in $\alpha(T_{BKT}) = 3$ [6].

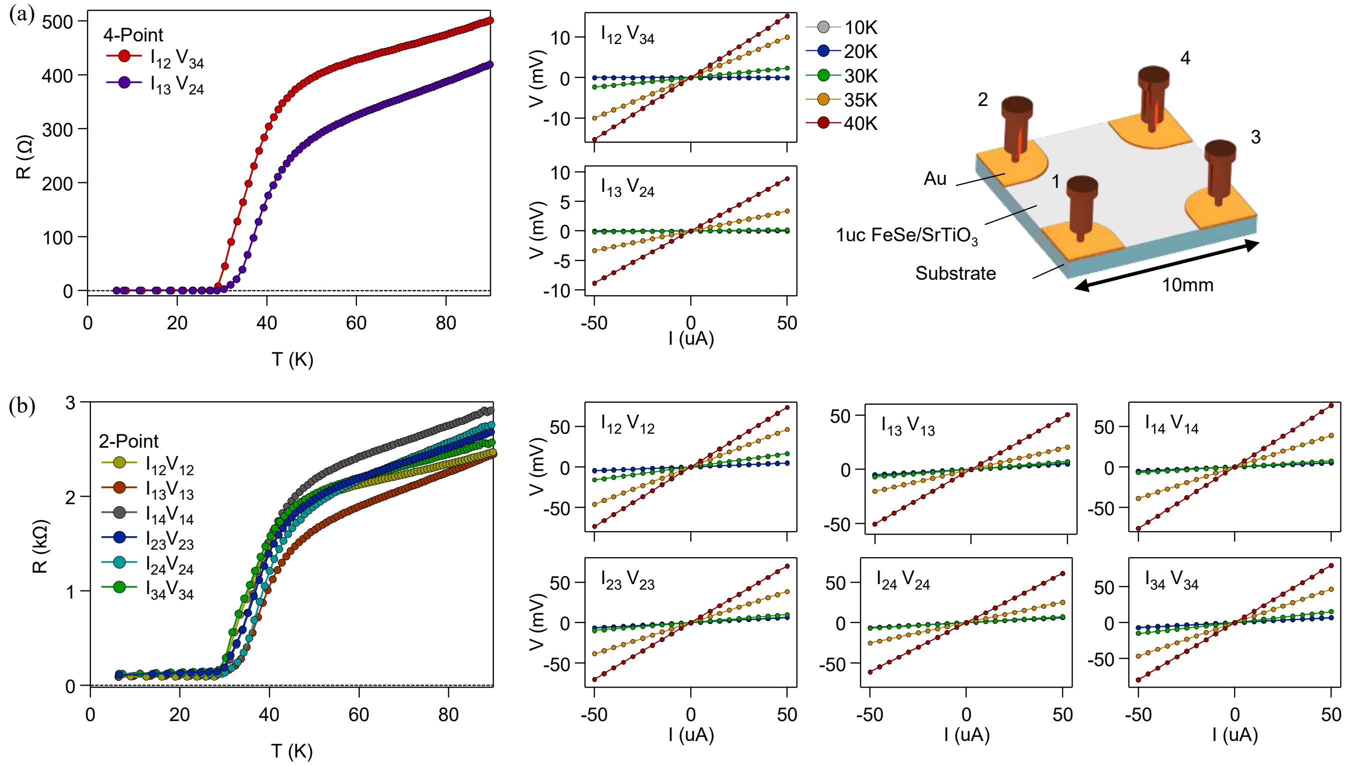

Figure S1. **Evaluation of the contact resistances during in situ $R(T)$ measurements on a representative 1uc FeSe/SrTiO$_3$ film.** (**a**) 4-point measurements taken along orthogonal directions in the Van der Pauw geometry. The left panel displays the resistance measured using the Delta mode while the right panels show the voltage response in current-pulse mode at various temperatures across the transition. The diagram in the upper right panel shows the index convention used for the contact probes. (**b**) Equivalent 2-point resistances (left panel) and V(I) behavior (right panels) measured between each pair of contacts, including lead and contact resistances.

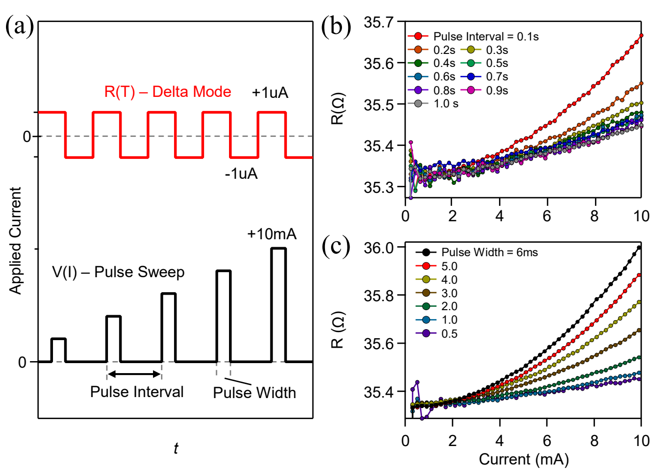

Figure S2. **Heating effects during V(I) measurements.** (**a**) Diagram showing measurement modes used for R(T) (red) and V(I) (black) measurements shown throughout the text. (**b,c**) Measured resistance of a representative 1uc FeSe/SrTiO$_3$ film held above T_0 as a function of applied current in Pulse Sweep mode. For shorter pulse intervals (**b**) or longer pulse widths (**c**) some heating effects are evident.

Above T_{BKT} the proliferation of thermally excited free vortices leads to a linear resistance from vortex flux flow, such that $\alpha(\mathrm{T}>T_{BKT}) = 1$.

At low applied currents the emergent flux-flow resistance is related to the density of thermally-populated free vortices n_F, which we can define in terms of a correlation length $\xi^2 = 1/(2\pi n_F)$, analogous to the Ginzburg-Landau coherence length ξ_0 for Cooper pairs; at separations less than ξ, vortices remain bounded in pairs, even above T_{BKT}. At T_{BKT}, ξ diverges, thus all vortices are paired. For comparison to *in situ* transport measurements, we can express this in terms of the excess conductivity $\Delta\sigma$ in the BKT vortex state compared to the normal state σ_n. Above T_{BKT} it can be shown [7] that the excess conductivity exhibits exponential behavior related to the density of thermally generated vortices:

$$\frac{\Delta\sigma_{BKT}}{\sigma_n} = \left(\frac{\xi}{\xi_0}\right)^2 = Ae^{b/\sqrt{t}}, \quad T_{BKT} < T < T_c. \quad (3)$$

Thus the intermediate vortex state may produce a substantially broadened superconducting transition.

Additionally, two-dimensional superconductors may intrinsically exhibit greatly enhanced amplitude fluctuations [8] which manifest as short-lived, uncondensed Cooper pairs above T_c that contribute to both the density of states and con-

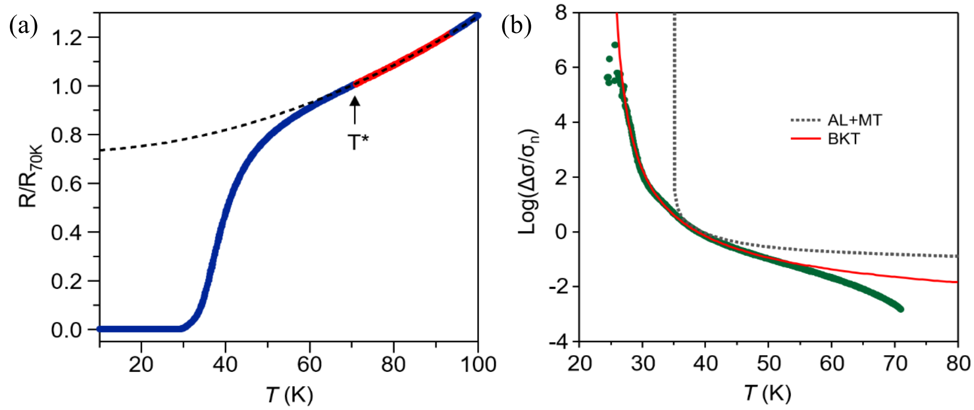

Figure S3. **Fitting of the superconducting transition to BKT and AL paraconductivity models.** (**a**) *in situ* resistivity data from Figs. 1 and 2 of the main text, normalized to the resistance at 70 K. (b) The excess conductivity extracted from the data in panel (a). Dashed black and red lines show fits to the AL+MT paraconductivity and BKT models, respectively.

duction. The contribution of thermally populated cooper pairs to the conduction is described by the Aslamazov–Larkin (AL) paraconductivity:

$$\Delta\sigma_{\mathrm{AL}} = \frac{e^2}{16\hbar}\frac{T_c}{T-T_c}, \quad T > T_c, \tag{4}$$

with an additional term for the Maki-Thomson correction [9, 10] included as

$$\Delta\sigma_{\mathrm{MT}} = \frac{e^2}{8\hbar}\frac{T_c}{T-(1+\delta)T_c}\ln\frac{T-T_c}{\delta T_c}, \quad T > T_c. \tag{5}$$

In Figure S3 we compare fits of the superconducting transition in single-layer $FeSe/SrTiO_3$ measured by *in situ* transport to the BKT and AL+MT models described by equations 4 and 5. Figure S3(a) shows R_s(T) for the single-layer film as presented in Figs 1-3 of the main text. The normal-state resistance (black dashed line) is extrapolated from Rs above T* (red region). Fig. S3(b) shows the normalized excess conductivity in log scale (green), along with fits to the BKT model (red line) and the AL paraconductivity (black dashed line). As shown, the AL+MT fitting fails to reproduce the shape of R_s(T) seen in our films, both at low temperatures approaching T_0 and the steeper downwards slope at higher temperatures.

III. MEASUREMENT AND EVALUATION OF THE SUPERCONDUCTING ENERGY GAP

Figure S4 outlines the procedure used to generate detailed temperature-dependent gap measurements as shown in Figure 2. The film is gradually warmed from 12-94 K while continuously measuring ARPES spectra at M [Fig. S4(d,e)]. The Fermi level is determined by periodically measuring reference spectra on the amorphous Au electrodes (in direct electrical and thermal contact with the FeSe film). Fig. S4(c) shows angle-integrated (normalized) spectra for Au at different temperatures through the sweep. The energy resolution and temperature are estimated based on a fitting of the integrated Au spectra to the Fermi function. Measured EDCs at k_F [Fig. S4(f) are symmetrized about E_F to generate the data in Fig. 2(a,b).

One approach to evaluating the superconducting energy gap Δ is to fit the symmetrized EDC's at E_F to a model spectral function with a self-energy in the form of

$$\Sigma(\mathbf{k},E) = -i\Gamma_1 + \frac{\Delta^2}{[E+\epsilon(\mathbf{k})+i\Gamma_0]}, \tag{6}$$

where Γ_0 is the inverse pair lifetime, Γ_1 describes the single-particle scattering rate, and $\epsilon(\mathbf{k})$ is the bare band dispersion. The corresponding spectral function is then calculated as

$$A(\mathbf{k},E) = -\frac{1}{\pi}\frac{\Sigma''(\mathbf{k},E)}{[E-\epsilon(\mathbf{k})-\Sigma'(\mathbf{k},E)]^2+\Sigma''(\mathbf{k},E)^2}, \tag{7}$$

and convolved with a gaussian with full width at half maximum (FWHM) matching the experimental energy resolution to produce a model spectral function for gap fitting. This method accounts for artificial broadening of the photoemission spectra due to energy resolution and scattering effects, and has been used previously in studies of high-T_c superconductors and monolayer $FeSe/SrTiO_3$ [11, 12].

At low temperatures, where the sample is deep within the superconducting state, Γ_0 can be reasonably assumed to be 0, and a fit of the form of Eqs. S5 and S6 can be performed reliably. Near the gap closing temperature and in the presence of superconducting fluctuations, however, the assumption that $\Gamma_0 = 0$ no longer holds, and a fitting of the form of Eqs. S5 and S6 becomes poorly constrained: both $\Delta = 0$ or an excessive Γ_0 produce fully "filled" spectral functions. As we are more

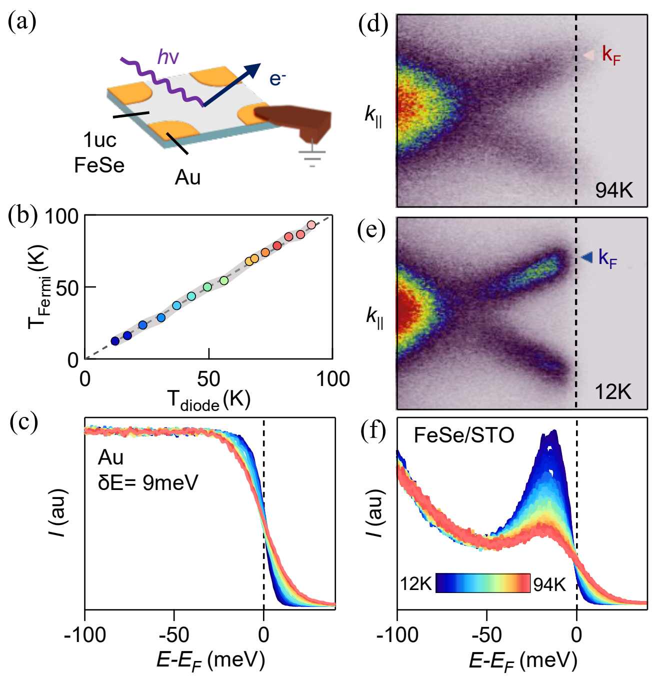

Figure S4. **ARPES gap measurements and temperature evaluation.** (**a**) Measurement configuration for ARPES gap measurements. The sample is grounded using a press contact built onto the sample manipulator. (**b**) The sample temperature evaluated from a fit to the Fermi edge of the Au electrodes, as shown in (**c**), compared to the sample diode reading. (**d-f**) Temperature evolution of the ARPES spectra at M. The data in Panel F is equivalent to that shown in Figure 2(b) without symmetrization.

concerned with the presence of an energy gap (as a signature of incoherent cooper pairs), we use instead the peak separation to characterize Δ(T) for the entire temperature range in the main text, particularly in Fig. 2(c). The gap-opening temperature T_Δ is identified as the maximum temperature at which separated quasiparticle peaks are distinguishable above the measurement noise [Fig. S5(c)].

To ensure that our estimation of T_Δ is not skewed by our methodology, we have tested using the spectral-function fitting approach as well, allowing Γ_0, Γ_1, and Δ to remain unconstrained fitting parameters, as shown in Figure S5.

IV. DATA FROM ADDITIONAL SAMPLES

The data shown in Fig. 4(b) and Fig. 4(c) of the main text is compiled from many single-layer FeSe/$SrTiO_3$ samples for which temperature-dependent transport data is available. Of these, low-temperature ARPES data were also available on five films, and temperature-dependent data for four. Figure S6 presents temperature-dependent symmetrized EDC's at k_F for the additional films not presented in the main text, but included in Fig. 4. T_Δ for each sample was determined via the same approach as used in Fig. 2 of the main text. Despite variation in the disorder strength, all films show qualitatively similar behavior to that of the film presented in Fig. 2, namely the distinct filling of spectral weight at E_F at low temperatures, as well as comparable T_Δ values.

Fig. S7 shows dR_s/dT data for the same selection of metallic (positive dR_s/dT at all temperatures) films presented in Fig.4(a). Fig. S7(a) shows full data out to 150 K, and Fig. S7(b) shows a zoom-in on the region near T^*.

[1] Takashi Uchihashi, Puneet Mishra, Masakazu Aono, and Tomonobu Nakayama, "Macroscopic Superconducting Current through a Silicon Surface Reconstruction with Indium Adatoms: $\mathrm{Si}(111)-(\sqrt{7}\times\sqrt{3})-\mathrm{In}$," Phys. Rev. Lett. **107**, 207001 (2011).

[2] Natalie Briggs, Brian Bersch, Yuanxi Wang, Jue Jiang, Roland J. Koch, Nadire Nayir, Ke Wang, Marek Kolmer, Wonhee Ko, Ana De La Fuente Duran, Shruti Subramanian, Chengye Dong, Jeffrey Shallenberger, Mingming Fu, Qiang Zou, Ya-Wen Chuang, Zheng Gai, An-Ping Li, Aaron Bostwick, Chris Jozwiak, Cui-Zu Chang, Eli Rotenberg, Jun Zhu, Adri C. T. van Duin, Vincent Crespi, and Joshua A. Robinson, "Atomically Thin Half-Van der Waals Metals Enabled by Confinement Heteroepitaxy," Nature Materials **19**, 637–643 (2020).

[3] Ronald Chwang, B.J. Smith, and C.R. Crowell, "Contact Size Effects on the van der Pauw Method for Resistivity and Hall Coefficient Measurement," Solid-State Electronics **17**, 1217 – 1227 (1974).

[4] N. D. Mermin and H. Wagner, "Absence of Ferromagnetism or Antiferromagnetism in One- or Two-Dimensional Isotropic Heisenberg Models," Phys. Rev. Lett. **17**, 1133–1136 (1966).

[5] J. M. Kosterlitz and D. J. Thouless, "Ordering, Metastability and Phase Transitions in Two-Dimensional Systems," Journal of Physics C Solid State Physics **6**, 1181–1203 (1973).

[6] J M Kosterlitz, "The Critical Properties of the Two-Dimensional xy Model," Journal of Physics C: Solid State Physics **7**, 1046–1060 (1974).

[7] L. Benfatto, C. Castellani, and T. Giamarchi, "Broadening of the Berezinskii-Kosterlitz-Thouless Superconducting Transition by Inhomogeneity and Finite-Size Effects," Phys. Rev. B **80**, 214506 (2009).

[8] Anatoly Larkin, Andrei Varlamov, and James Annett, "Theory of Fluctuations in Superconductors," Physics Today **59** (2006).

[9] Kazumi Maki, "The Critical Fluctuation of the Order Parameter in Type-II Superconductors," Progress of Theoretical Physics **39**, 897–906 (1968).

[10] J. W. P. Hsu and A. Kapitulnik, "Superconducting Transition, Fluctuation, and Vortex Motion in a Two-Dimensional Single-Crystal Nb Film," Phys. Rev. B **45**, 4819–4835 (1992).

[11] Q. Song, T. L. Yu, X. Lou, B. P. Xie, H. C. Xu, C. H. P. Wen, Q. Yao, S. Y. Zhang, X. T. Zhu, J. D. Guo, R. Peng, and D. L. Feng, "Evidence of Cooperative Effect on the Enhanced Superconducting Transition Temperature at the FeSe/$SrTiO_3$ Interface," Nature Communications **10**, 758 (2019).

[12] M. R. Norman, M. Randeria, H. Ding, and J. C. Campuzano, "Phenomenology of the Low-Energy Spectral Function in High-T_c Superconductors," Phys. Rev. B **57**, R11093 (1998).

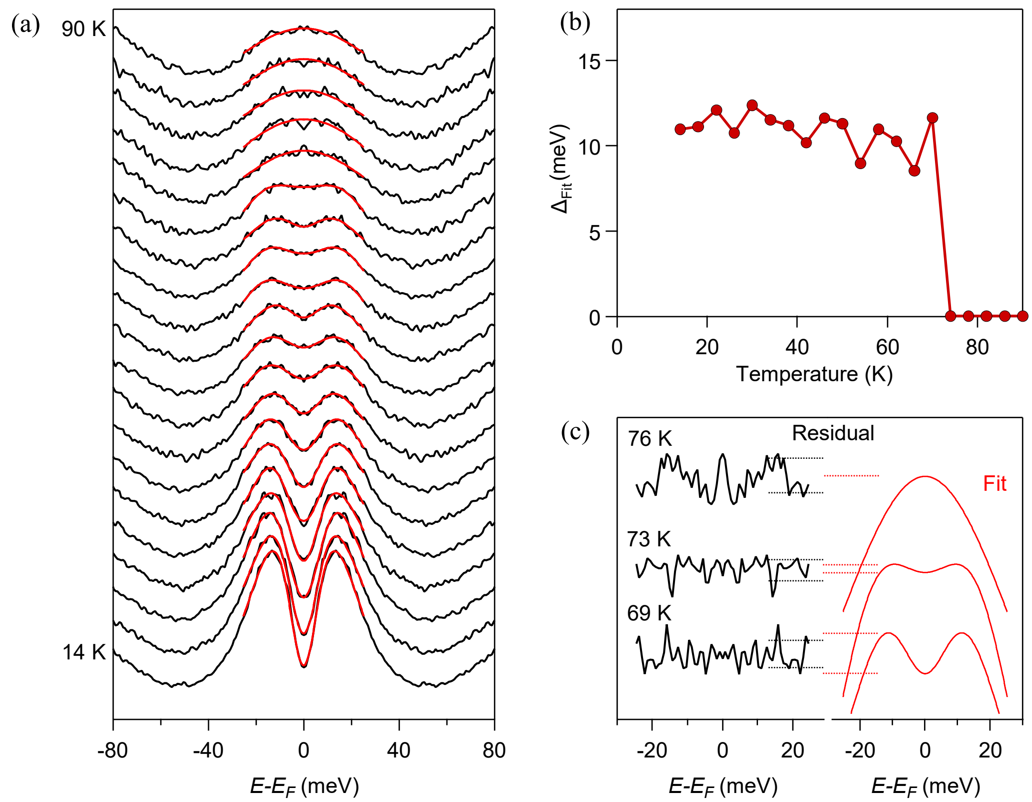

Figure S5. **Fitting of the superconducting gap** (**a**) Temperature-dependent EDC's duplicated from Fig. 2(b), along with fits to the spectral function of Eqs. 6 and 7. (**b**) Δ(T) from fits in panel (a) (**c**) Comparison of EDC gap fits (red) to the residual noise (black) for temperatures near T_Δ.

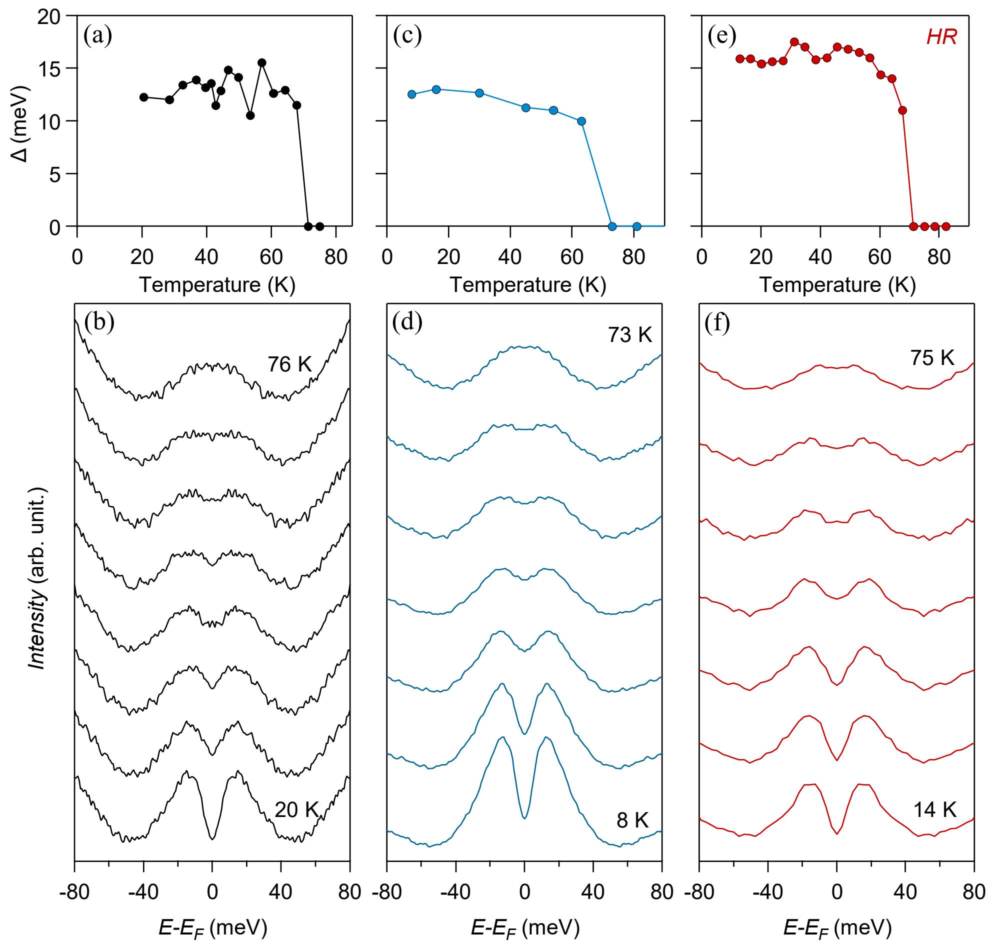

Figure S6. **Temperature-dependent EDC's for additional single-layer FeSe/$SrTiO_3$ films.** Data shown for 3 separate films not previously presented in the main text, including temperature-dependent EDC's at k_F (b,d,f) and corresponding Δ(T) based on quasiparticle peak separation (a,c,e). For films (a) and (e), only a sampling of the total measured EDC's are presented.

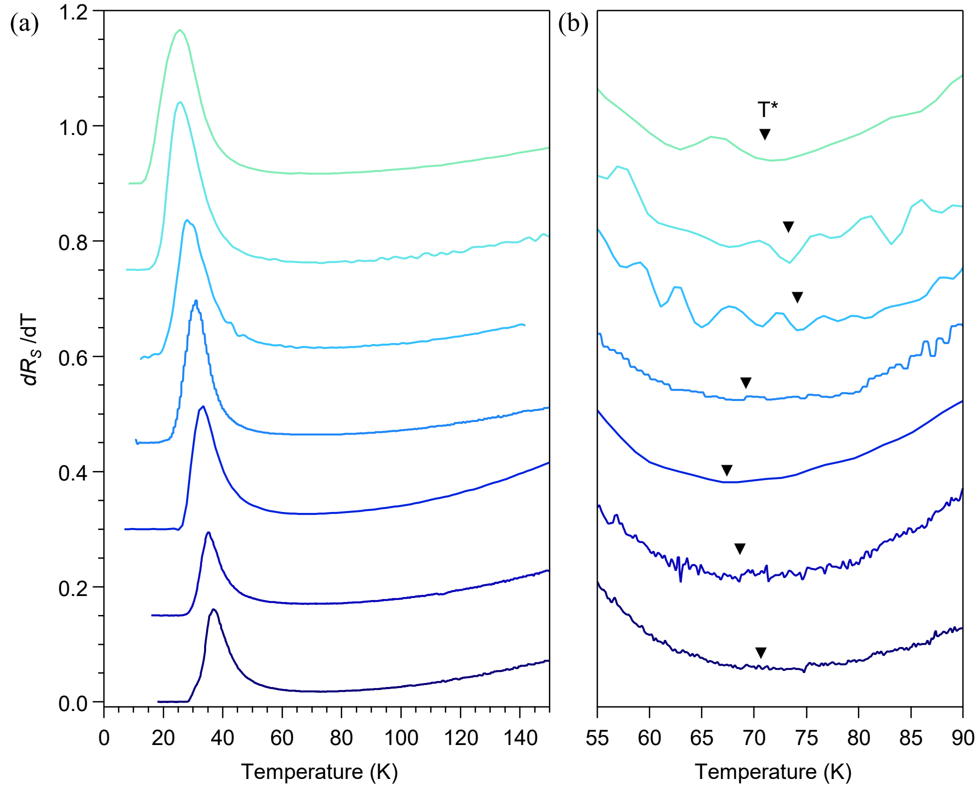

Figure S7. **dR_s/dT for additional superconducting single-layer FeSe/$SrTiO_3$ films.** (**a**) dR_s/dT for the metallic, superconducting films for which R_s(T) was presented in Fig. 4(a) of the main text. (**b**) Zoom-in near $T_\triangle$ for the data shown in (a). Arrows indicate the extracted values of $T_\triangle$ for each curve.